

Contents lists available at ScienceDirect

# Petroleum Science

journal homepage: www.keaipublishing.com/en/journals/petroleum-science



# Original Paper

# Adsorption behavior of CO<sub>2</sub>/H<sub>2</sub>S mixtures in calcite slit nanopores for CO<sub>2</sub> storage: An insight from molecular perspective



Cheng Qian <sup>a, b</sup>, Zhen-Hua Rui <sup>a, b, c, d, \*</sup>, Yue-Liang Liu <sup>a, b, c, \*\*</sup>, Kai Du <sup>a, b</sup>, Chen Liu <sup>a, b</sup>, Yang Zhao <sup>a, b, c</sup>, Xiao-Min Ma <sup>e</sup>

- <sup>a</sup> State Key Laboratory of Petroleum Resources and Engineering, China University of Petroleum, Beijing, 102249, China
- <sup>b</sup> College of Petroleum Engineering, China University of Petroleum, Beijing, 102249, China
- <sup>c</sup> College of Carbon Neutrality Future Technology, China University of Petroleum, Beijing, 102249, China
- <sup>d</sup> College of Petroleum, China University of Petroleum-Beijing at Karamay, Karamay, 83400, Xinjiang, China
- <sup>e</sup> College of Mining Engineering, Taiyuan University of Technology, Taiyuan, 030024, Shanxi, China

#### ARTICLE INFO

# Article history: Received 5 September 2023 Received in revised form 18 March 2024 Accepted 20 March 2024 Available online 22 March 2024

Edited by Yan-Hua Sun

Keywords: Adsorption behavior CO<sub>2</sub>/H<sub>2</sub>S binary mixtures Molecular perspective Calcite slit nanopores CO<sub>2</sub> sequestration

#### ABSTRACT

It is acknowledged that injecting CO<sub>2</sub> into oil reservoirs and saline aquifers for storage is a practical and affordable method for CO<sub>2</sub> sequestration. Most CO<sub>2</sub> produced from industrial exhaust contains impurity gases such as H<sub>2</sub>S that might impact CO<sub>2</sub> sequestration due to competitive adsorption. This study makes a commendable effort to explore the adsorption behavior of CO<sub>2</sub>/H<sub>2</sub>S mixtures in calcite slit nanopores. Grand Canonical Monte Carlo (GCMC) simulation is employed to reveal the adsorption of CO2, H2S as well as their binary mixtures in calcite nanopores. Results show that the increase in pressure and temperature can promote and inhibit the adsorption capacity of CO2 and H2S in calcite nanopores, respectively. CO2 exhibits stronger adsorption on calcite surface than H<sub>2</sub>S. Electrostatic energy plays the dominating role in the adsorption behavior. Electrostatic energy accounts for 97.11% of the CO2-calcite interaction energy and 56.33% of the H<sub>2</sub>S-calcite interaction energy at 10 MPa and 323.15 K. The presence of H<sub>2</sub>S inhibits the CO<sub>2</sub> adsorption in calcite nanopores due to competitive adsorption, and a higher mole fraction of H<sub>2</sub>S leads to less CO<sub>2</sub> adsorption. The quantity of CO<sub>2</sub> adsorbed is lessened by approximately 33% when the mole fraction of H<sub>2</sub>S reaches 0.25. CO<sub>2</sub> molecules preferentially occupy the regions near the pore wall and H<sub>2</sub>S molecules tend to reside at the center of nanopore even when the molar ratio of CO<sub>2</sub> is low, indicating that CO<sub>2</sub> has an adsorption priority on the calcite surface over H<sub>2</sub>S. In addition, moisture can weaken the adsorption of both CO2 and H2S, while CO2 is more affected. More interestingly, we find that pure CO<sub>2</sub> is more suitable to be sequestrated in the shallower formations, i.e., 500–1500 m, whereas CO<sub>2</sub> with H<sub>2</sub>S impurity should be settled in the deeper reservoirs.

© 2024 The Authors. Publishing services by Elsevier B.V. on behalf of KeAi Communications Co. Ltd. This is an open access article under the CC BY-NC-ND license (http://creativecommons.org/licenses/by-nc-nd/

4.0/).

#### 1. Introduction

Excessive consumption of fossil fuels has caused a surge in carbon dioxide (CO<sub>2</sub>) emissions (Metz et al., 2005; O'Neill, 2020). In 2021, the CO<sub>2</sub> emissions from energy increased to 36.3 Gt to reach their highest ever annual level (International Energy Agenc, 2022; Liu and Rui, 2022). Meanwhile, the environmental problems caused by excessive CO<sub>2</sub> emissions have also attracted increasing attention all over the world. The fifth assessment report of the United Nations

E-mail addresses: ruizh@cup.edu.cn (Z.-H. Rui), yueliang@cup.edu.cn (Y.-L. Liu).

Intergovernmental Panel on Climate Change (IPCC) proposed that the 450 ppm CO<sub>2</sub> equivalent concentration would be achieved by 2100 (the temperature rise should be controlled within 1.5 °C) (Liu and Rui, 2022). CO<sub>2</sub> capture, utilization, and storage (CCUS) technology will be an essential technique to control carbon dioxide emissions and mitigate climate problems (Bui et al., 2018; Cui et al., 2018; Tyne et al., 2021). Some CCUS techniques have been proposed for carbon neutrality such as CO<sub>2</sub>-enhanced gas recovery (CO<sub>2</sub>-EGR), CO<sub>2</sub>-enhanced coal bed methane recovery (CO<sub>2</sub>-ECBM), CO<sub>2</sub>-enhanced geothermal systems (CO<sub>2</sub>-EGS), gas hydrate based CO<sub>2</sub> storage (Hu et al., 2022; Shi et al., 2018; Sun et al., 2023). One of the most effective CCUS techniques includes storing CO<sub>2</sub> in deep saltwater aquifers and drained oil and gas reserves (Iglauer, 2017;

<sup>\*</sup> Corresponding author.

<sup>\*\*</sup> Corresponding author.

Vilarrasa and Carrera, 2015). Injecting CO<sub>2</sub> into oil and gas reservoirs combines CO<sub>2</sub> sequestration and CO<sub>2</sub> enhanced oil recovery (CO<sub>2</sub>-EOR) to bring economic benefits to oil companies (Clark and Santiso, 2018; Li H. et al., 2021; Liu S. et al., 2022; Liu Y. et al., 2022).

Apart from the location of CO<sub>2</sub> storage, another major barrier that hinders the widespread application of CCUS should be the significant expense of CO<sub>2</sub> separation from CO<sub>2</sub>-rich industrial waste gas (Cui et al., 2021a; Kolle et al., 2021; Lu et al., 2016). The process of removing CO<sub>2</sub> from industrial waste gas and purifying it would consume a significant amount of energy (Keith et al., 2018; Wei et al., 2015). The reduction of the requirement for  $CO_2$  purity would be a feasible way to minimize costs in all capture processes (Wang et al., 2015). Hence, lowering the standard of impurity gas in CO<sub>2</sub> injected into the formation can significantly reduce the expenditure of the whole CO<sub>2</sub> geo-storage project (Wang et al., 2016; Yu et al., 2021). As one of the primary CO<sub>2</sub> sources, industrial exhaust, when captured and separated, can be injected into geological formations to achieve carbon sequestration and emission reduction. However, the impurity gases present in the separated CO2-rich industrial exhaust, such as SO2, H2S, CH4, CO, continue to exert an influence on carbon sequestration. Among these, hydrogen sulfide (H2S) is a typical gas found in industrial waste gas and depleted reservoirs (Cholewinski et al., 2016; Hutcheon, 1999; Talman, 2015). On the outskirts of Edmonton, a depleted oil reservoir started to pump gases with compositions ranging from  $83\% H_2S + 14\% CO_2$  to  $2\% H_2S + 95\% CO_2$  (Zhang et al., 2011). In the Western Canada Sedimentary Basin, the concentration of dissolved CO<sub>2</sub> at the forefront of the fluid flow might exceed 50% (Ghaderi et al., 2011). H<sub>2</sub>S contained in the stored CO<sub>2</sub> and originally in the depleted oil and gas reservoirs should not be ignored because it makes the CCUS projects much more complicated and expensive. The toxicity of H<sub>2</sub>S is another factor concerning public safety, and that requires a different set of regulations. Therefore, the influence of hydrogen sulfide on the adsorption characteristics of CO2 in formation is worthy of being investigated. The study of the impact of impurities like H<sub>2</sub>S on CO<sub>2</sub> sequestration is very limited, while most of the literature pays heavy attention to mineral dissolutions, multiphase fluid transport, phase behavior, and gas solubility in the formation water (Bolourinejad and Herber, 2014; Ji and Zhu, 2013; Li D. et al., 2021; Li and Jiang, 2020). Li and his coworkers (Li D. et al., 2021; Li and Jiang, 2020) studied the combined effect of native H<sub>2</sub>S and other impurity gases existing in CO<sub>2</sub> gas flow on CO<sub>2</sub> storage in saline aquifer. They found that H<sub>2</sub>S dissolution caused a reduction in the concentration of injected gas at the two-phase interface and weakened the convection process. The presence of H<sub>2</sub>S in CO<sub>2</sub> flows could result in two-phase flow, and the bubble and dew pressures drop with increasing H2S concentration in H2S/CO2 mixes (Ji and Zhu, 2013). Bolourinejad and Herber (2014) experimentally examined the impacts of H<sub>2</sub>S on salt precipitation and mineral dissolution in the process of CO<sub>2</sub> flooding and found that the presence of H<sub>2</sub>S damages the permeability due to the aggravation of salt and mineral precipitation.

Subsurface aquifers and depleted oil and gas reserves are regarded as the two main CO<sub>2</sub> storage sites. In both brine aquifers and oil reservoirs, calcite is a very prevalent mineral component (Cui et al., 2021b; Jayasekara et al., 2020). When CO<sub>2</sub> is sequestrated, it is inevitable to discuss the interaction between CO<sub>2</sub> containing H<sub>2</sub>S impurity gases and calcite due to the highly probable existence of H<sub>2</sub>S gas in the injected CO<sub>2</sub> or formation. While GCMC simulation is a widely used research approach, we applied GCMC simulation to reveal the adsorption behavior of individual components (CO<sub>2</sub> and H<sub>2</sub>S) and their binary combination in this work (Deng et al., 2022; Liu et al., 2019b; Wang et al., 2021). Previous research examined the effect of contaminants in CO<sub>2</sub> gas on its geological storage using molecular modeling. Chen et al. (2018)

found that the presence of H<sub>2</sub>S reduces the interfacial tension of CO<sub>2</sub>-water and improves the contact angle in the CO<sub>2</sub>/water/silica system. The reduction of interfacial tension enhances the CO<sub>2</sub>-water interaction and CO<sub>2</sub> dissolution trapping, while the promotion of contact angle weakens the CO<sub>2</sub> adsorption on the silica wall. Kamath and Potoff (2006) adopted the originally optimized Monte Carlo algorithm to predict the phase behavior of CO<sub>2</sub>/H<sub>2</sub>S/CH<sub>4</sub> mixtures, and the simulation results are in good agreements with experimental data. Fazelabdolabadi and Alizadeh-Mojarad (2016) probed the structural anisotropy of various hydrocarbon fluid/H<sub>2</sub>S/CO<sub>2</sub>/H<sub>2</sub>O combinations and discovered the ordered arrangement of pure H<sub>2</sub>O/H<sub>2</sub>S/CO<sub>2</sub> within the adsorption molecules on the carbonate wall.

However, limited studies concentrated on the adsorption characteristics of individual CO<sub>2</sub>, H<sub>2</sub>S, and binary mixtures. This study examines the adsorption performance of CO<sub>2</sub>/H<sub>2</sub>S mixture in calcite slit nanopores by conducting Monte Carlo simulations. A wide range of temperatures (293.15-383.15 K) and pressures (0-30 MPa) is tested to cover the conditions of conventional reservoirs. The pore size is set at the micropore level (< 2 nm) because micropores contribute significantly to the adsorption of hydrocarbons and other gases in the formation with ultra-low permeability and developed micro-nano pores (Zhang et al., 2020). The influence of pressure, temperature, the mole fraction of gas, and moisture content on the adsorption capacity of CO2, and H2S in calcite nanopores were examined, and the competitive adsorption behavior of (CO<sub>2</sub> + H<sub>2</sub>S) binary mixtures was also presented. The conclusion of this work is expected to be beneficial to the competitive adsorption of multicomponent gas in nanopores and the effects of impurities on CO<sub>2</sub> sequestration.

#### 2. Models and methodology

# 2.1. Calcite slit nanopore model

The calcite slit nanopore model is composed of two calcite slabs, and each slab has six calcite layers. The single calcite layer with a thickness of 18.21 Å is obtained by cutting the (1 0 1 4) crystallographic face first and the supercell operation following. The X, Y, and Z dimensions of the simulation calcite model are set as 32.38, 34.93, and 49.55 Å, respectively, as shown in Fig. 1, and the width of the pore (Z-direction) is fixed at 13.0 Å. In all directions, periodic boundary conditions are implemented. The calcite and two gas molecules ( $CO_2$  and  $H_2S$ ) are rigid entities, and the charges of individual atoms and the lengths of the bonds are listed in Table 1.

# 2.2. Force field

A force field is essential for molecular simulation, and a suitable force field can accurately calculate the interaction and potential energy between different molecular structures. COMPASS II (Condensed-phase optimized molecular potentials for atomistic simulation studies) force field is an optimized version of COMPASS force field and permits the precise and simultaneous estimation of gas-phase and condensed-phase features such as structure, equation of state, and vibration frequency over a wide range of molecules and polymers (Liu et al., 2019a; Luo et al., 2020). The COMPASS force field is the first high-quality force field integrating organic and inorganic material parameters (Sun, 1998). The COM-PASS II is adopted to perform the entire simulation using the Materials Studio software package based on the previous literature (Sun and Wang, 2020; Wang et al., 2018). Plenty of research adopted the COMPASS II force field in calcite-gas molecule-water systems and the outcomes are consistent with the experimental data (Li et al., 2022; Zhang et al., 2021). The basic mathematical



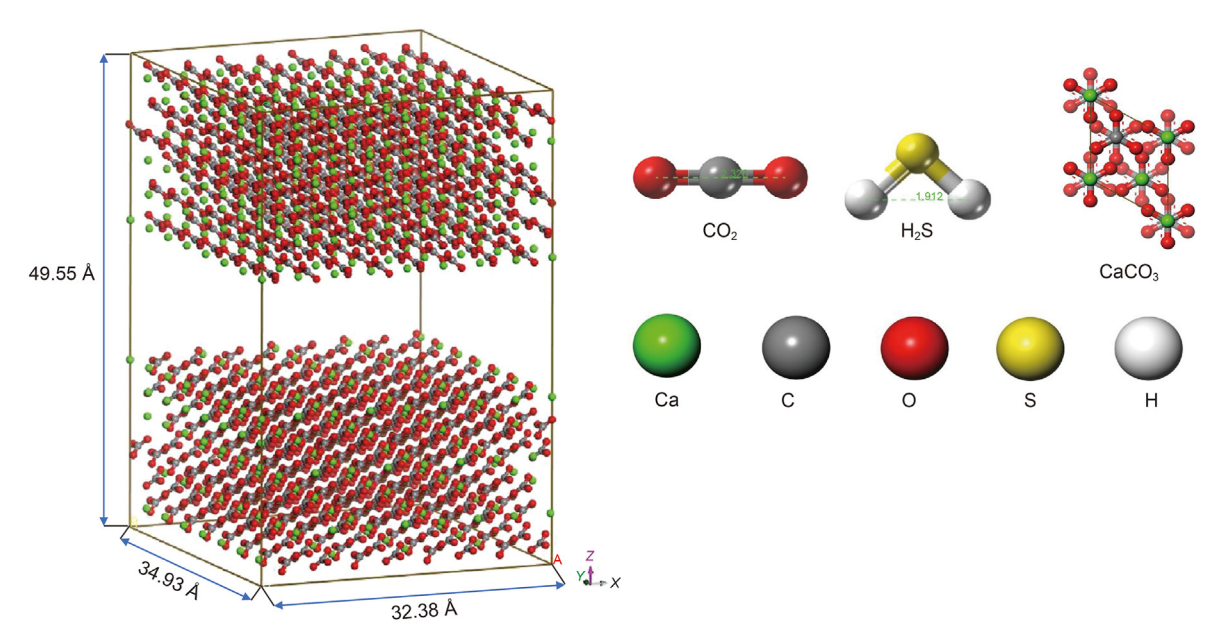


Fig. 1. Model schematic of a calcite nanopore with a pore size of is 13 Å and the individual molecules in the simulation. Color scheme: green-Ca ion; gray-C; red-O; yellow-S; white-H

**Table 1** Molecular structure parameters of CO<sub>2</sub> and H<sub>2</sub>S.

Molecule	Atom	Charge, e	Bond length, Å
CO <sub>2</sub>	С	0.80	2.320
	0	-0.40	
$H_2S$	S	-0.338	1.912
	Н	0.169	

expression of COMPASS II force field is shown as follows (Sun et al., 2016):

$$E_{\text{total}} = E_b + E_{\theta} + E_{\phi} + E_{\chi} + E_{bb'} + E_{b\theta} + E_{b\phi} + E_{\theta\theta'} + E_{\theta\phi} + E_{\theta\theta'\phi} + E_{\text{vdW}} + E_{\text{ele}}$$

$$(1)$$

The sum of valence terms, including diagonal and off-diagonal cross-couplings and nonbonded interaction terms, represents the entire potential energy in the COMPASS II force field.  $E_b$ ,  $E_\theta$ ,  $E_\phi$ , and  $E_\chi$  are the valence terms for the bond, angle, torsion, and out-of-plane angle coordinates, respectively.  $E_{bb'}$ ,  $E_{b\theta}$ ,  $E_{b\phi}$ ,  $E_{\theta\theta'}$ ,  $E_{\theta\phi}$ , and  $E_{\theta\theta'\phi}$  are the valence terms for cross-coupling terms between internal coordinates (Sun et al., 1998). Coulombic potentials, which describe the electrostatic interaction, and Lennard-Jones 9-6, which describes the van der Waals interaction, serve to define the nonbonded potential. The non-bonded potential is on behalf of intermolecular interaction. The electrostatic interaction and van der Waals interaction are expressed as follows (McQuaid et al., 2004):

$$E_{\text{vdW}} = \sum E_{\text{LJ}} \left[ 2 \times \left( \frac{r_{ij}^0}{r_{ij}} \right)^9 - 3 \times \left( \frac{r_{ij}^0}{r_{ij}} \right)^6 \right]$$
 (2)

$$E_{\rm ele} = \sum_{ij} \frac{q_i q_j}{4\pi\varepsilon_0 r_{ij}} \tag{3}$$

#### 2.3. GCMC simulation

The adsorption behavior is investigated through the GCMC algorithm, and each GCMC simulation is carried out under the Fix pressure mode with a total calculation step of  $2\times 10^7$ . The first ten million steps are set for the equilibration of the calcite-gas molecule system and the subsequent ten million steps are developed to compute the adsorption process's thermodynamic characteristics. The electrostatic interaction and the van der Waals interaction are characterized by the Ewald & Group algorithm and the Atom-based algorithm with a cutoff radius of 1.55 nm, respectively. The simulation utilizes fugacity instead of pressure to perform  $\text{CO}_2$  and  $\text{H}_2\text{S}$  adsorption, and the fugacity of  $\text{CO}_2$  and  $\text{H}_2\text{S}$  is determined using the Peng–Robinson equation.

#### 3. Results and discussion

#### 3.1. The isotherms of $CO_2$ and $H_2S$ adsorption

# 3.1.1. Adsorption isotherms

The adsorption isotherms of pure CO<sub>2</sub> and H<sub>2</sub>S in calcite nanopores at various pressures and temperatures are indicated in Fig. 2. Pure CO<sub>2</sub> can adsorb more readily in calcite nanopores at higher pressures but is less effective at higher temperatures. In calcite nanopores, the effects of pressure and temperature on H2S adsorption are similar to those of CO<sub>2</sub>. The adsorption isotherms of H<sub>2</sub>S rise dramatically compared to CO<sub>2</sub>. The ability of the calcite nanopores to adsorb gas is improved as the pressure rises. The high temperature improves the thermal motion of the CO<sub>2</sub> and H<sub>2</sub>S, increasing the molecule's kinetic energy as a consequence. Therefore, gas molecules are less inclined to adsorb on the nanopores, decreasing the adsorption amounts. Additionally, under identical circumstances, the maximum adsorption amount of H<sub>2</sub>S is larger than that of CO<sub>2</sub>, and the maximum adsorption capacity of CO<sub>2</sub> is more sensitive to variations in temperature and pressure than that of H2S.

#### 3.1.2. Density distributions

Fig. 3 illustrates the density profiles of CO<sub>2</sub> and H<sub>2</sub>S at 323.15 K in

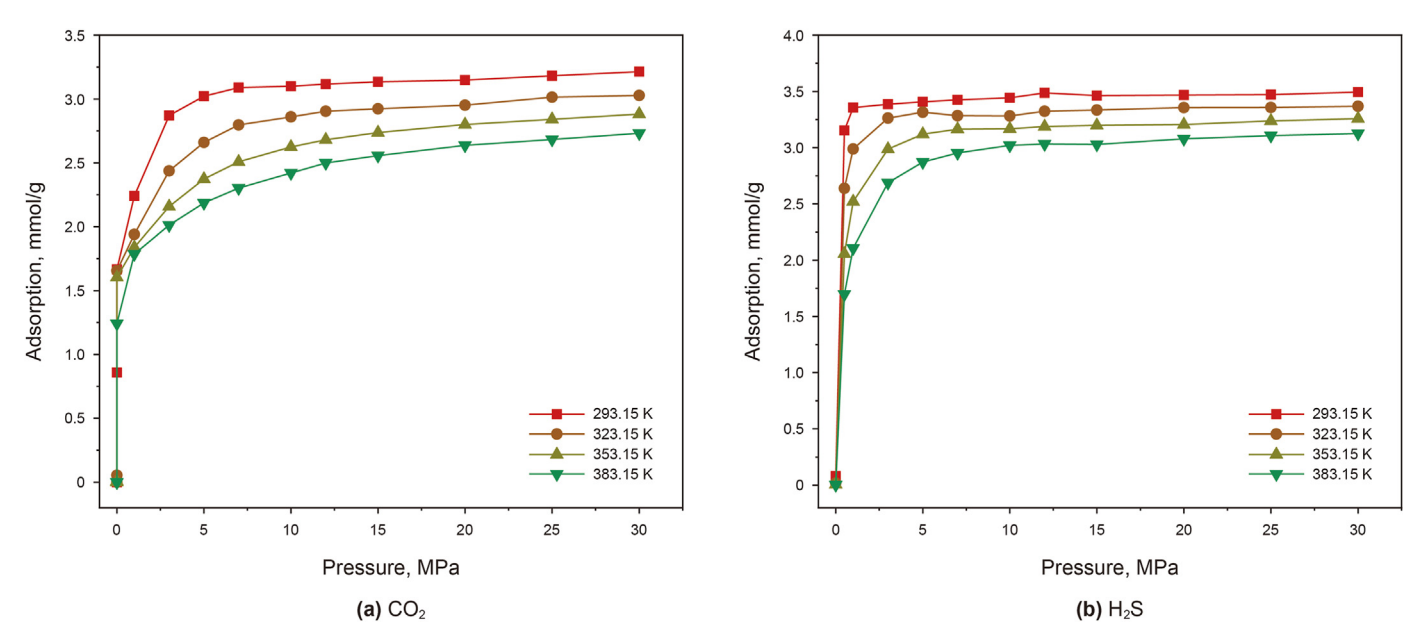


Fig. 2. Adsorption isotherms of CO<sub>2</sub> and H<sub>2</sub>S within calcite nanopores.

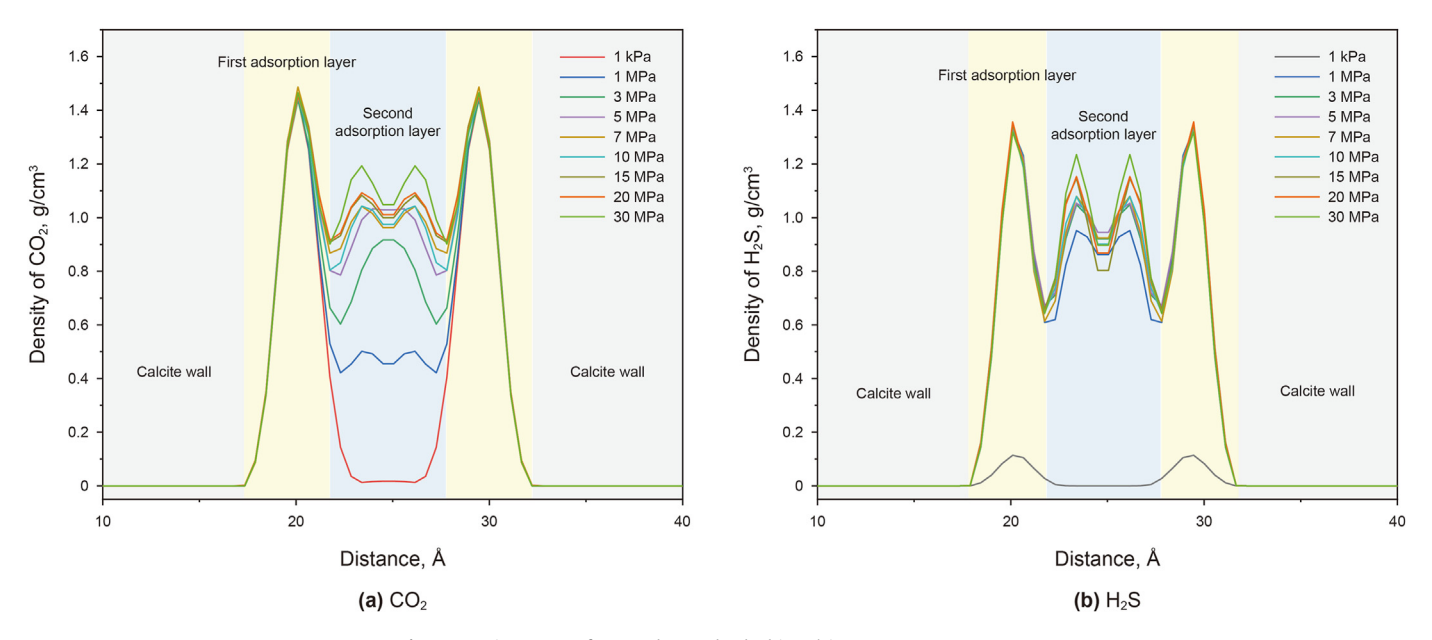


Fig. 3. Density curves of  $CO_2$  and  $H_2S$  adsorbed in calcite nanopores at 323.15 K.

calcite nanopores along the Z-axis. In general, the density profile of two pure gases rises when the pressure increases, and gas molecular layers adsorbed on the calcite surface would transform from single to double layers with the increasing pressure. Similar to the first adsorbed layer, the density of the second adsorbed layer also increases as the pressure ascends. As seen in Fig. 3(a), only one adsorbing layer for  $CO_2$  can be observed when the pressure is lower than 5 MPa, while  $H_2S$  forms double-layer adsorption on the calcite surface at 1 MPa (Fig. 3(b)), The influence of pressure is consistent with Section 3.1.1, and the adsorption of  $H_2S$  increases more sharply than that of  $CO_2$  as the pressure increases. Compared with  $H_2S$ , the initial  $CO_2$  adsorption layer has a greater density than the  $H_2S$  layer, suggesting that the adsorption amount of  $CO_2$  in the first adsorption layer is larger than that of  $H_2S$ . The adsorbed gas molecules in the closest layer usually present stronger interactions, and  $CO_2$ 

shows a tighter interaction with calcite.

The  $CO_2$  and  $H_2S$  density profiles in calcite nanopores at 5 MPa along the Z-axis are illustrated in Fig. 4. As the temperature increases, the density of pure  $CO_2$  and  $H_2S$  tends to decline, while the first and second adsorption layers of two pure gases both decrease correspondingly. In addition, the two adsorption peaks of the second adsorption layer gradually evolved into a single adsorption peak when the temperature increases. The second adsorption layer of  $CO_2$  is more affected by temperature than  $H_2S$  based on the density variation. As mentioned in Section 3.1.1, the elevation in temperature amplifies the thermal motion of gas molecules, consequently diminishing their adsorption density within nanopore.

Furthermore, changes in the secondary adsorption layer reflect the effects of temperature more clearly. The rise in temperature

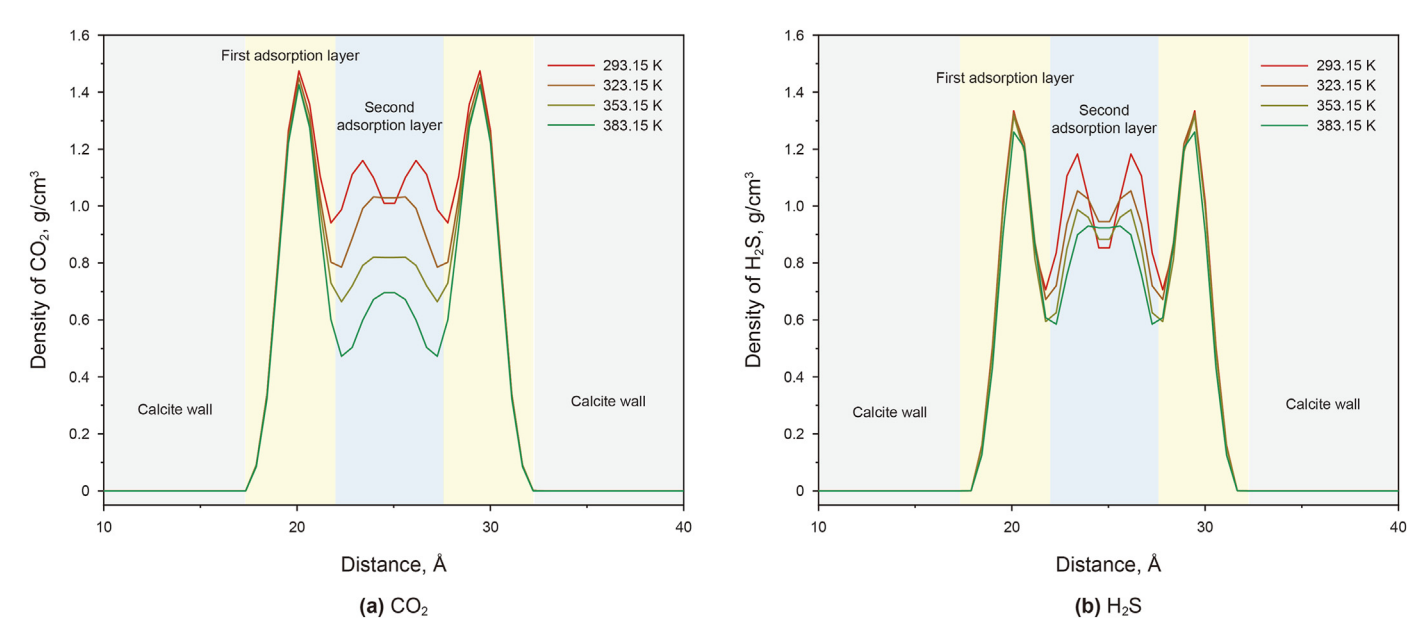


Fig. 4. Density curves of CO<sub>2</sub> and H<sub>2</sub>S adsorbed in calcite nanopores at 5 MPa.

diminishes the density of the second adsorption layer, transforming the double adsorption peak into a single adsorption peak. This is primarily attributable to the reduction in density leading to a decrease in the number of molecules, insufficient to sustain the formation of a bilayer adsorption. Simultaneously, it is also a consequence of the diminished attraction exerted by the calcite surface on gas molecules within the second adsorption layer. The peak value of the first adsorption layer has little variation in CO<sub>2</sub> and H<sub>2</sub>S density curves. It is because of the strong attraction between the first adsorption layer and the calcite. The calcite surface exhibits pronounced variations in the interactions with molecules in different adsorption layers, and the fundamental cause lies in the distance from the surface; the closer to the surface, the stronger the attraction, with less susceptibility to temperature influence. Conversely, greater distances are subject to more substantial temperature effects. In addition, CO<sub>2</sub> has a greater density in the first adsorption layer than H2S and H2S prefers to form double-layer adsorption than CO2 at high temperatures. As for CO2 sequestration, the low pressure and high temperature are not conducive to raise storage. The increase in pressure can effectively strengthen the adsorption and CO<sub>2</sub> storage in calcite formation.

#### 3.1.3. Radial distribution function

The radial distribution function (RDF) refers to the distribution frequency of other particles in the space around a given particle (how far away from the given particle). RDF reflects the intensity of calcite and gas molecule interactions. Meanwhile, RDF has a consistent trend over a range of temperature and pressure settings. The RDFs of CO<sub>2</sub> and CaCO<sub>3</sub> at 323.15 K and 1 MPa are displayed in Fig. 5. The first chart indicates the RDF of CO<sub>2</sub> and the Ca<sup>2+</sup> of CaCO<sub>3</sub> and the latter chart is the RDF of  $CO_2$  and the  $CO_3^2$  of  $CaCO_3$ . The maximum of CO<sub>2</sub>-Ca<sup>2+</sup>(CaCO<sub>3</sub>) is higher than those of CO<sub>2</sub>- $CO_3^{2-}(CaCO_3)$ , which shows that  $CO_2$  favors the adsorption with the  $Ca^{2+}$  of calcite. The peak value of  $Ca^{2+}(CaCO_3)$ -O( $CO_2$ ) emerges at 2.26 Å, and that of  $Ca^{2+}$  ( $CaCO_3$ )-C( $CO_2$ ) emerges at 3.30 Å, suggesting that the distance between the oxygen atom of carbon dioxide and  $Ca^{2+}$  is less than that of the carbon atom and  $Ca^{2+}$ . Therefore, the strongest interaction within the CO<sub>2</sub>-calcite system belongs to the intermolecular forces between the oxygen atom of carbon dioxide and the calcium ion in calcite, which is in accord

with the previous study (Javasekara et al., 2020).

Fig. 6 displays the RDF curves of  $CO_2$  and  $CaCO_3$  (calcite). Fig. 6(a) and (b) indicate the RDF of  $CO_2$  and the  $Ca^{2+}$  of  $CaCO_3$  and that of  $CO_2$  and the  $CO_3^{2-}$ , respectively. In Fig. 6(a), the highest values of RDFs of three kinds of atom in  $CaCO_3$  and  $S(H_2S)$  are apparently higher than the peak value of the three kinds of the atom and the hydrogen atom. It can be inferred that the surfer atom with negative charge is more prone to attach to a calcite surface than the hydrogen atom with positive charge. Taking the ranges between the S of  $H_2S$  and three kinds of atoms in  $CaCO_3$  into consideration, the smaller the distance means the stronger the interaction between the two atoms, and the gap space between the surfer atom and calcium ion reaches a minimum value. In a word, the interaction between the surfer atom and calcium ion is strongest in the  $H_2S$ -calcite system.

The RDF curves of  $Ca^{2+}(CaCO_3)$ - $CO_2$  and  $Ca^{2+}(CaCO_3)$ - $H_2S$  are plotted in Fig. 7. The maximum values of the two RDF curves are 4.59 and 2.25 and the distances between the calcium ion and two gas molecules are 2.26 and 3.62 Å, correspondingly. It is obvious that the affinity between  $CO_2$  and  $Ca^{2+}$  is better than that of  $H_2S$  and  $Ca^{2+}$ , indicating a more readily interaction of  $CO_2$  molecules with  $CaCO_3$ .

#### 3.1.4. Interaction energy

The intermolecular interaction energy between calcite and gas molecules is considered as the interaction energy ( $E_{\rm int}$ ) and the interaction energy consists of the van der Waals energy ( $E_{\rm vdw}$ ) and electrostatic energy ( $E_{\rm elec}$ ). The interaction energy values between calcite and pure  ${\rm CO_2/H_2S}$  and the percentage denoting the proportion of  $E_{\rm elec}$  and  $E_{\rm vdw}$  in the  $E_{\rm int}$  are presented in Table 2. The absolute values of the interaction energy reveal the intensity of the attraction between gas molecules and calcite, which is indicated by its negative value. The interaction energy of calcite- ${\rm CO_2}$  dominantly comes from the electrostatic energy that accounts for 97.11% of  $E_{\rm int}$ . As for the calcite- ${\rm H_2S}$  system, the strengths of  $E_{\rm vdw}$  and  $E_{\rm elec}$  are similar and have a proportion of 43.67% and 56.33%, respectively. The  $E_{\rm int}$  of calcite- ${\rm CO_2}$  is higher than that of calcite- ${\rm H_2S}$ , showing a more intense attraction in the calcite- ${\rm CO_2}$  system, which explained the more readily interaction of  ${\rm CO_2}$  molecules with the  ${\rm CaCO_3}$ .

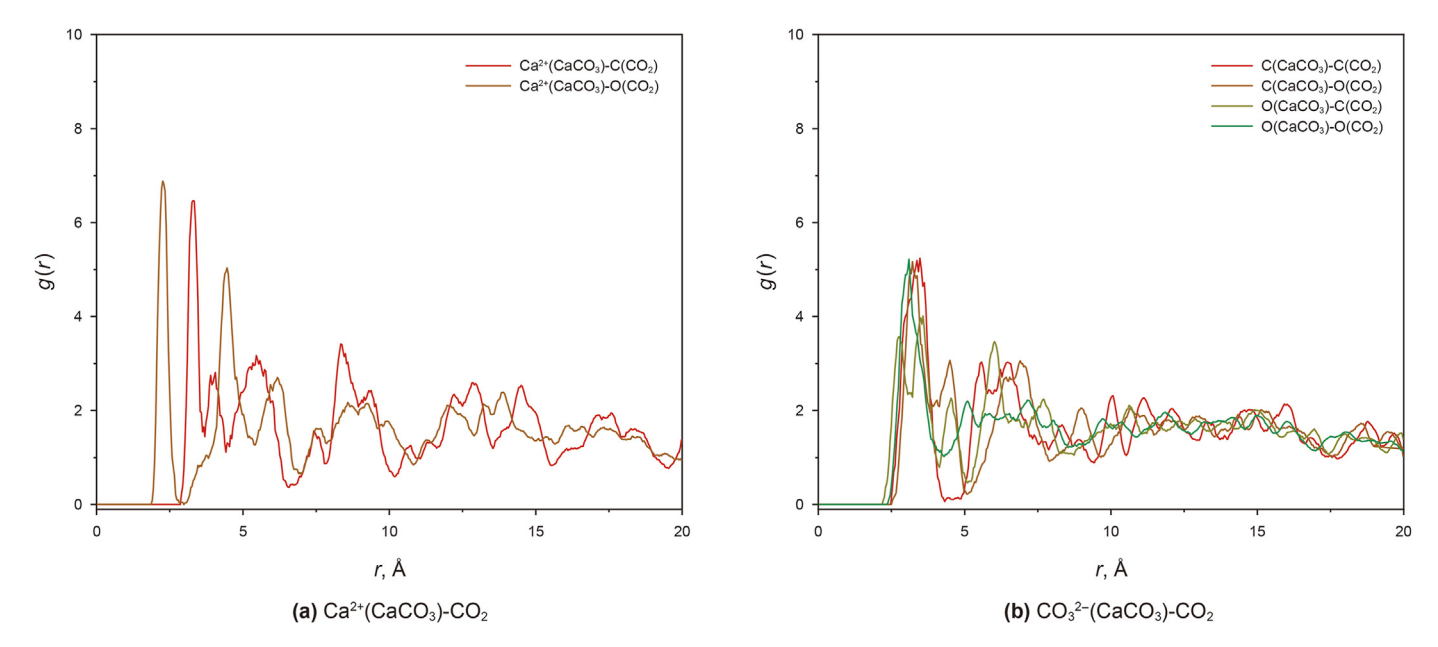


Fig. 5. The radial distribution function between the atom of CO2 and the atoms of CaCO3 at 323.15 K and 1 MPa.

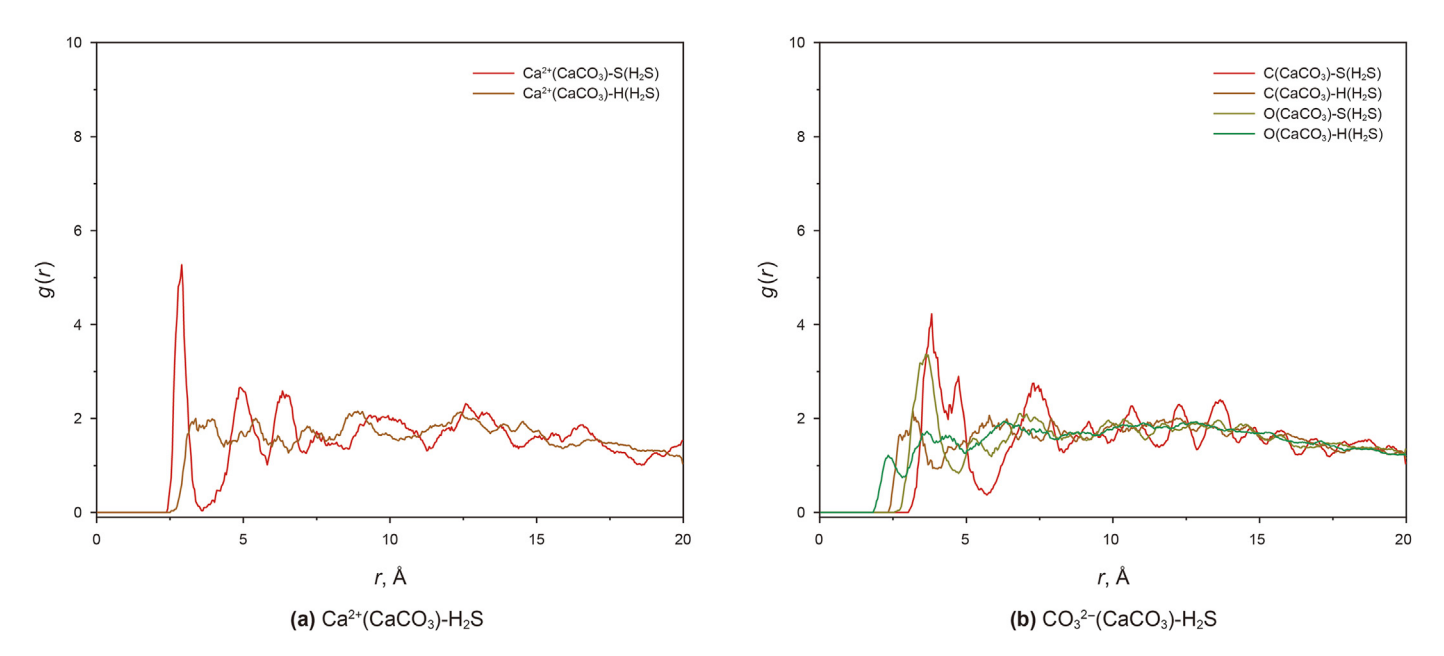


Fig. 6. The radial distribution function between the atom of H<sub>2</sub>S and the atoms of CaCO<sub>3</sub> at 323.15 K and 1 MPa.

# 3.1.5. Adsorption orientation of CO<sub>2</sub> and H<sub>2</sub>S

The angle  $\theta$  marked in Fig. 8(a) formed by the CO<sub>2</sub>/H<sub>2</sub>S molecules and the calcite contact was calculated to determine the orientations of CO<sub>2</sub> and H<sub>2</sub>S. The CO<sub>2</sub> molecules adsorbed on the calcite surface show an angle range of 15°–45°. The distribution of angles suggests that CO<sub>2</sub> molecules tend to recline on calcite surfaces, as shown in Fig. 8(b). The principal consideration is the strong affinity between the O atom of CO<sub>2</sub> and Ca<sup>2+</sup> of CaCO<sub>3</sub>. As for the  $\theta$  of H<sub>2</sub>S, the frequency distribution is the highest at 0° and the larger angle is companied by the lower frequency distribution, suggesting that the axis of H<sub>2</sub>S is inclined to keep a parallel or small angle with the calcite adsorption surface. Explanation for this phenomenon is that the sulfur atoms are always preferentially adsorbed on the calcite surface and two hydrogen atoms with weaker charge have a nearly

equal interaction with the surface force of calcite.

#### 3.2. Adsorption isotherms of CO<sub>2</sub>/H<sub>2</sub>S mixture

#### 3.2.1. Adsorption isotherms and average isosteric heat

The H<sub>2</sub>S content in different sites and injection methods varied dramatically. Generally, the concentration of H<sub>2</sub>S in CO<sub>2</sub> injected into oil and gas reservoirs or deep saline aquifers does not exceed 10% (Alpermann et al., 2016; Li et al., 2017). However, in an effort to minimize the emissions of H<sub>2</sub>S and CO<sub>2</sub>, Canada has implemented active sour gas injection projects involving the injection of solutions or dense fluids. In such projects, the H<sub>2</sub>S component can constitute 2%–83% of the total gas injected (Bachu et al., 2005; Bachu and Bennion, 2009). It should be noted that, in conventional

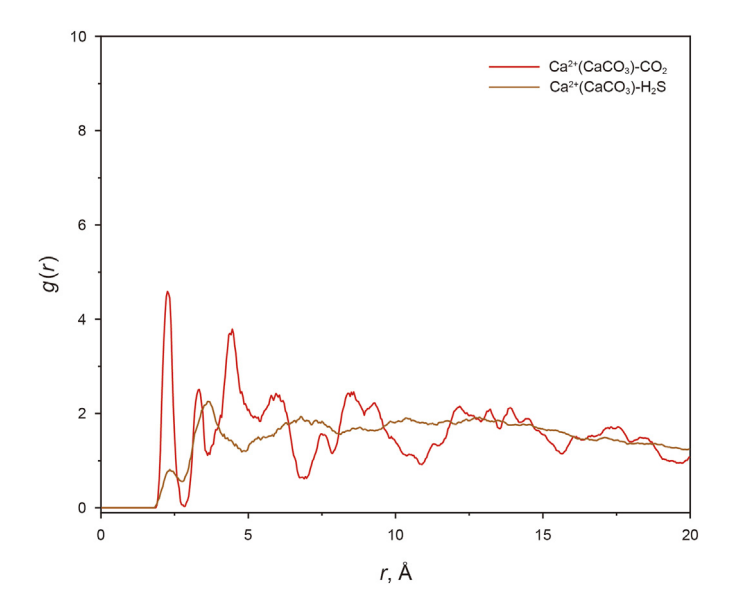


Fig. 7. The RDFs between  $CO_2/H_2S$  molecules and calcium ion of  $CaCO_3$  at 323.15 K and 1 MP<sub>2</sub>

**Table 2** Interaction energy between CaCO<sub>3</sub> and CO<sub>2</sub>, H<sub>2</sub>S systems (10 MPa, 323.15 K).

Pure gas	Interaction	Interaction energy, kcal/mol			Percentage, %	
	$E_{\text{vdv}}$	$E_{ m elec}$	Eint	$E_{\rm vdv}$	E <sub>elec</sub>	
Calcite-CO <sub>2</sub> Calcite-H <sub>2</sub> S	-59.92 -738.94	-2012.22 -952.98	-2072.14 -1691.92	2.89 43.67	97.11 56.33	

natural gas reservoirs, the content of  $H_2S$  typically ranges from 2% to 70% (Bolourinejad and Herber, 2014; Ji and Zhu, 2013; Zhang et al., 2011). Consequently, the actual content of  $H_2S$  varies significantly between different locations during field operations. In order to fully characterize the competitive adsorption processes of  $CO_2$  verse  $H_2S$  under varied  $H_2S$  concentrations, the molar concentrations of  $CO_2$  and  $H_2S$  was assigned as 0%, 25%, 50%, 75%, and 100%, respectively.

The adsorption isotherms and average isosteric heat of  $CO_2$  and  $H_2S$  at the temperature of 323.15 K are plotted in Fig. 9(a) and (b). The adsorption capacity of  $CO_2$  and  $H_2S$  in calcite nanopores rises with the ascension of its mole fraction in binary mixes. When the mole fraction of  $CO_2$  is 0.75, the quantity of  $CO_2$  adsorbed is about two-thirds that of pure  $CO_2$ . The quantity of  $CO_2$  adsorbed is reduced by approximately 14% when the  $CO_2$  molar ratio falls from 0.5 to 0.25, indicating a faster decline in the adsorption capacity at a relatively high mole fraction of  $CO_2$ .

Unlike pure  $CO_2$ ,  $CO_2$  in binary mixtures reaches its maximum adsorption under lower pressure, while pure  $H_2S$  forms maximum adsorption more rapidly than  $H_2S$  binary mixtures. Then,  $CO_2$  adsorption isotherms exhibit a modest decrease as the pressure continues to increase with the presence of  $H_2S$ . Meanwhile, a mild rise occurs in the adsorption curves of  $H_2S$  accordingly. After the system pressure climbs to about 5 MPa, the amount of  $CO_2$  adsorbed starts to increase as  $H_2S$  adsorbed begins to decrease progressively. The existence of  $H_2S$  does affect the adsorption amount of  $CO_2$  in calcite nanopores due to the competitive adsorption, which would cut down the amount of  $CO_2$  sequestered in calcite rock. A higher mole fraction of  $H_2S$  would lead to less  $CO_2$  sequestration.

As shown in Fig. 9, the average isosteric heat of CO<sub>2</sub> adsorption process declines with the increases in pressure and mole proportion of CO<sub>2</sub>, while the average isosteric heat of H<sub>2</sub>S adsorption increases as the pressure and mole ratio of H<sub>2</sub>S ascend gradually. The adsorption potential of both gases is also directly influenced by the pressure and molar ratio. More specifically, when the adsorption amount of two gas molecules increases due to the changes in pressure and molar ratio, the average isosteric heat of CO<sub>2</sub> and H<sub>2</sub>S increases and decreases respectively. The differing energy levels of the gas molecules in the multiple adsorption layers account for the contradictory experimental findings and the impact of pressure and gas mole ratio on energy value would be discussed in detail in Section 3.2.3.

# 3.2.2. Density distributions

The density distribution of CO<sub>2</sub> and H<sub>2</sub>S with various mole fractions at 10 MPa and 323.15 K was shown in Fig. 10. The density profile of CO<sub>2</sub> and H<sub>2</sub>S in binary mixture generally increases with the increase in gas mole fractions. CO<sub>2</sub> molecules in the binary

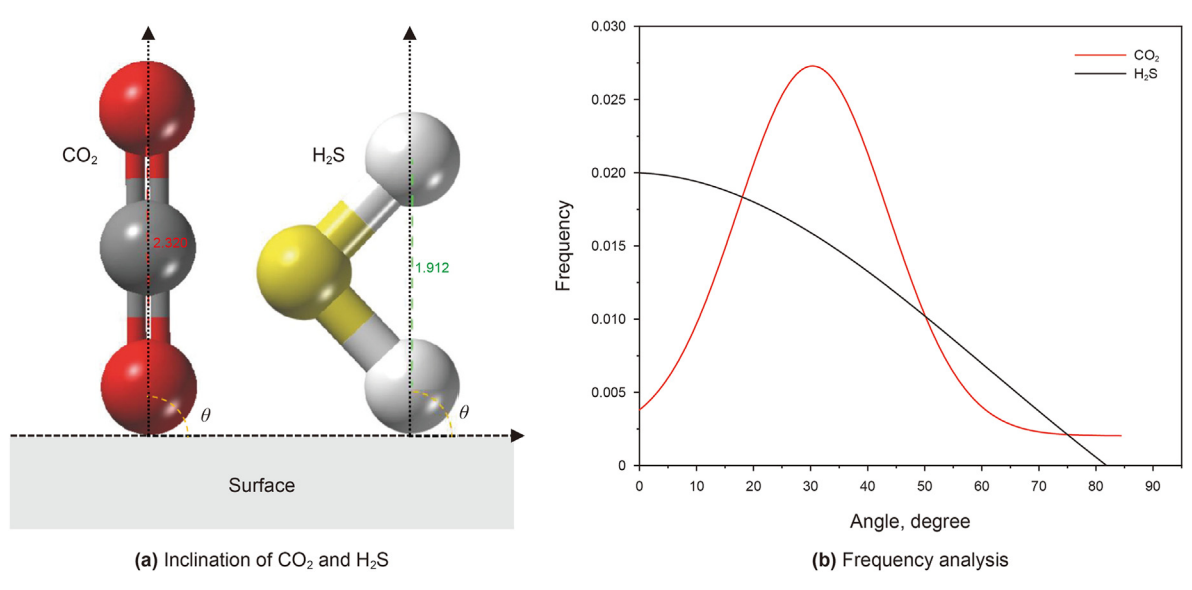
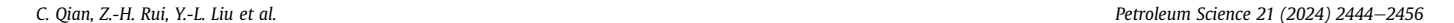


Fig. 8. Schematic diagram for the inclination of CO<sub>2</sub> and H<sub>2</sub>S, and frequency analysis for the angle  $\theta$  of CO<sub>2</sub> and H<sub>2</sub>S at 10 MPa and 323.15 K.



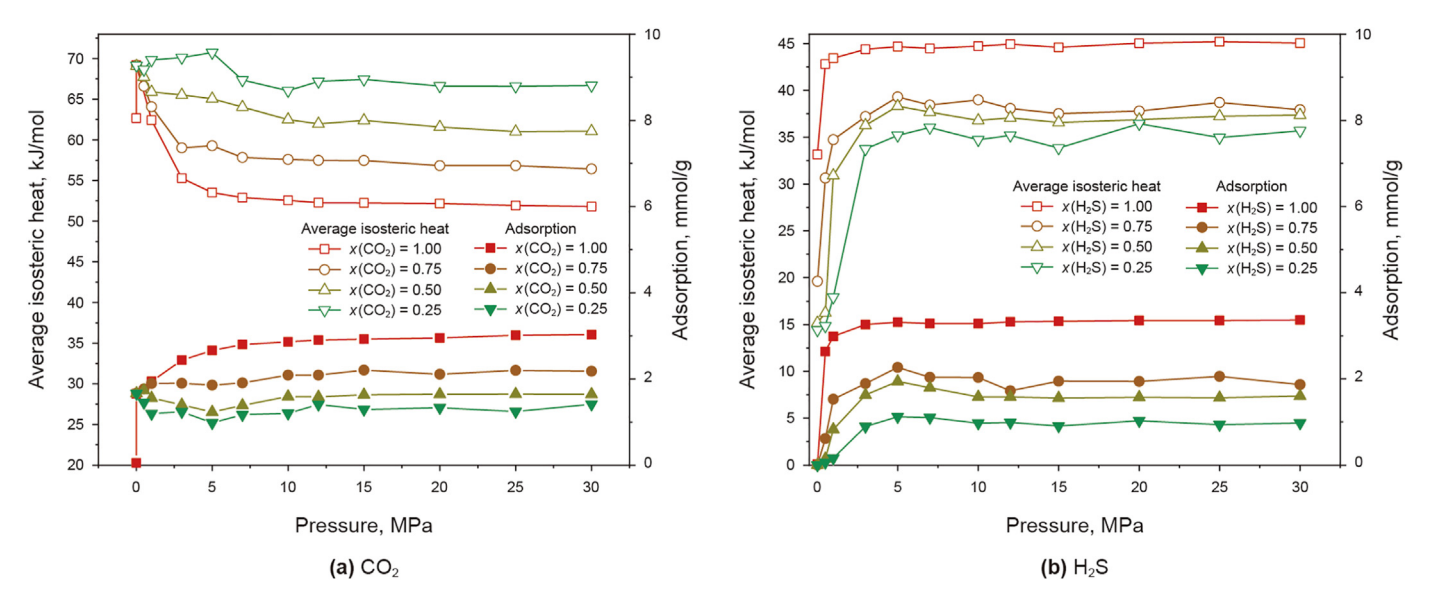


Fig. 9. Adsorption isotherms and average isosteric heat of CO<sub>2</sub> and H<sub>2</sub>S at 323.15 K (x(CO<sub>2</sub>) and x(H<sub>2</sub>S) are mole fractions of CO<sub>2</sub> and H<sub>2</sub>S in CO<sub>2</sub>/H<sub>2</sub>S mixture at the initial state).

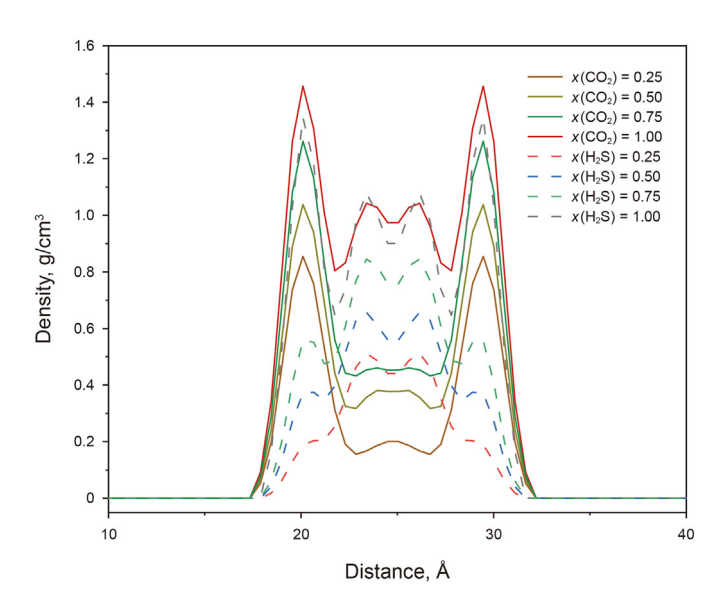


Fig. 10. Density profiles of  $CO_2$  and  $H_2S$  in calcite nanopores with different mole fractions (10 MPa, 323.15 K).

mixture always tend to form monolayer adsorption in calcite pore walls and the density profiles of  $H_2S$  would transform from monolayer to double layers when comparing the binary mixture with the density distribution of pure gas. For all simulations of  $CO_2/H_2S$  mixture in calcite nanopores, as shown in Fig. 11,  $CO_2$  molecules preferentially occupy the regions on both sides of the pores and  $H_2S$  molecules prefer to fill up the middle part of the pores according to the density profiles graphics. The density profiles of  $CO_2/H_2S$  mixtures imply that  $CO_2$  interacts more favorably with calcite surfaces than  $H_2S$ . According to the results of RDF and interaction energy, the attraction between  $CO_2$  and calcite is stronger than that of the calcite- $H_2S$  system. It implies that  $CO_2$  has the propensity to settle on the  $CaCO_3$  surface, and  $H_2S$  forms a weaker adsorption layer in areas away from the  $CaCO_3$  surface.

#### 3.2.3. Potential energy distribution

The potential energy distribution profiles of CO<sub>2</sub> and H<sub>2</sub>S with

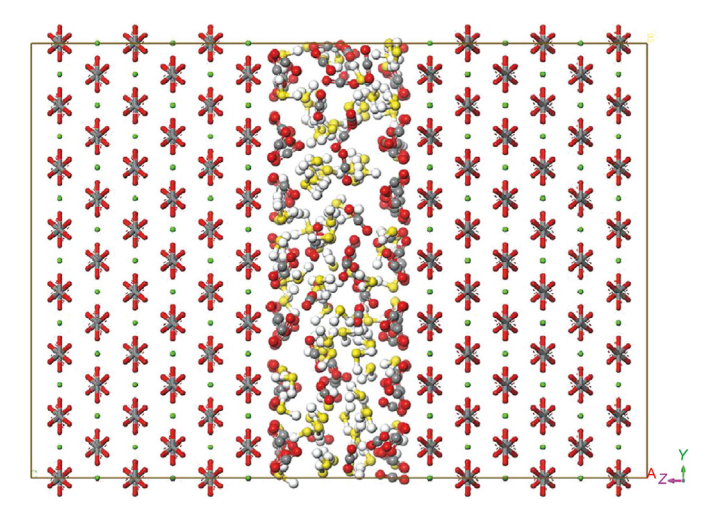


Fig. 11. Schematic diagram for the distribution of  $CO_2$  and  $H_2S$  molecules in calcite nanopores at  $x(CO_2)=0.5$  (10 MPa, 323.15 K).

various mole fractions at 10 MPa and 323.15 K are plotted in Fig. 12. As the mole fraction of the CO<sub>2</sub>/H<sub>2</sub>S combination in calcite nanopores increases, the distribution of potential energy evolves in the opposite direction. The peaks of CO<sub>2</sub> lines progressively shift to the right as the CO<sub>2</sub> ratio increases, and the peak value of the lower energy site and higher energy site fall and rise, respectively. Changes in energy distribution show that the adsorption of CO<sub>2</sub> in calcite nanopores progressively transforms from lower energy adsorption to higher energy sites as the CO<sub>2</sub> mole fraction rises. While the peak positions of H<sub>2</sub>S curves gradually slide to the lower energy sites with the presence of H<sub>2</sub>S. The extremum with lower energy increases and the extremum with higher energy declines with the rise of the H<sub>2</sub>S proportion. Meanwhile, the distribution probability of CO<sub>2</sub> in low-energy states is always greater than that in high-energy states, and the potential energy distribution of H<sub>2</sub>S is opposite to that of CO<sub>2</sub>.

The variation in the potential energy distribution of CO<sub>2</sub> and H<sub>2</sub>S molecules accounts for the different trends of average isosteric heat in CO<sub>2</sub> and H<sub>2</sub>S adsorption. If the initial energy of CO<sub>2</sub> is identical, a higher energy CO<sub>2</sub> molecule in equilibrium means a lower average



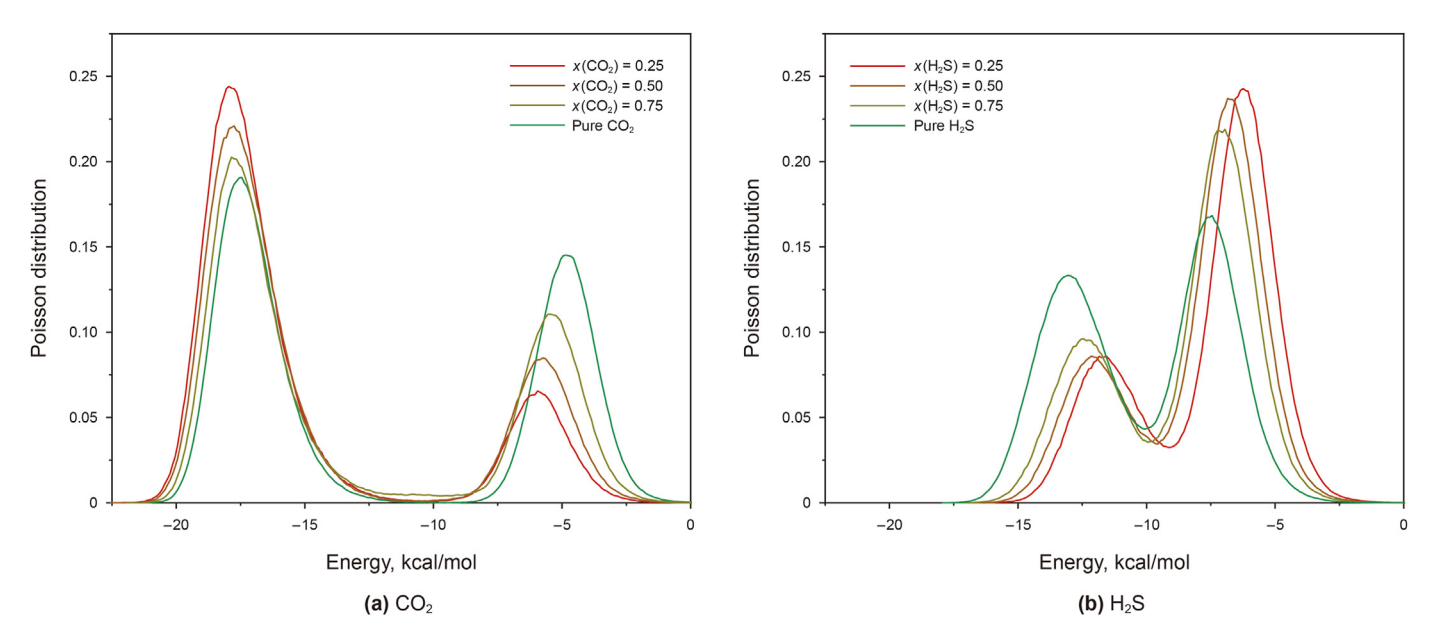


Fig. 12. Potential energy distribution of CO<sub>2</sub> and H<sub>2</sub>S in calcite nanopores with different mole fractions (10 MPa, 323.15 K).

isosteric heat. Based on simulation results, the alteration in energy of CO<sub>2</sub> and H<sub>2</sub>S in binary mixture matches the trend of the average isosteric heat as the gas mole fraction increases. In general, the energy and average adsorption strength of CO2 and H2S molecules in the binary mixture decreases and increases as the gas mole ratio increases separately. The double-layer adsorption of CO<sub>2</sub> and H<sub>2</sub>S is the primary cause of this phenomenon. CO<sub>2</sub> adsorbed in the first layer has lower energy and the excess CO<sub>2</sub> in the second adsorption layer exhibits higher energy. Owing to the saturation adsorption of the first layer, as the molar concentration of CO2 increases, the increased CO<sub>2</sub> molecules will settle more in the second adsorption layer. The increment of CO<sub>2</sub> in the secondary adsorption layer leads to an enhancement of the potential energy of CO2 molecules and CO<sub>2</sub> molecules as higher energy is less stable. Therefore, CO<sub>2</sub> adsorbing on the calcite surface will be more stably sequestered in the reservoir, and the CO<sub>2</sub> molecules in the second adsorption layer with higher energy are more easily desorbed. For H<sub>2</sub>S double-layer adsorption, the first adsorption layer of H<sub>2</sub>S similarly has lower energy, while the energy of the second adsorption layer is comparatively higher. In the case of pure H<sub>2</sub>S adsorption, the energy distribution is at its lowest state since, at this juncture, the proportion of H<sub>2</sub>S molecules in the first adsorption layer is maximized. With an increase in the concentration of H<sub>2</sub>S in the mixture, both the density of H<sub>2</sub>S molecules in the first and second adsorption layers escalates (as depicted in Fig. 10). However, the additional H<sub>2</sub>S molecules tend to be more prominently distributed in the first adsorption layer, thereby resulting in an overall upward trend in the energy of H<sub>2</sub>S molecules.

# 3.3. Adsorption selectivity of $CO_2$ over $H_2S$

To define the selective adsorption characteristics of  $CO_2/H_2S$  combination in calcite nanopores, we introduce the adsorption selectivity of  $CO_2$  over  $H_2S$ , which can be expressed as (Liu and Hou, 2020):

$$S_{\text{CO}_2/\text{H}_2\text{S}} = \frac{x_{\text{CO}_2}/x_{\text{H}_2\text{S}}}{y_{\text{CO}_2}/y_{\text{H}_2\text{S}}} \tag{4}$$

where  $x_{CO_2}$  and  $x_{H_2S}$  indicate the mole fractions of  $CO_2$  and  $H_2S$ 

adsorbed, respectively, in the first layer;  $y_{\text{CO}_2}$  and  $y_{\text{H}_2\text{S}}$  denote the mole fractions of  $\text{CO}_2$  and  $\text{H}_2\text{S}$  adsorbed, respectively, in the second layer. If  $S_{\text{CO}_2/\text{H}_2\text{S}}$  is greater than 1, it means that  $\text{CO}_2$  has the adsorption priority on the calcite surface over  $\text{H}_2\text{S}$  (Huang et al., 2022; Liu et al., 2016).

The adsorption selectivity of  $CO_2$  over  $H_2S$  in calcite nanopores is illustrated in Fig. 13. Each of the computed adsorption selectivity values exceeds 1, which demonstrates that  $CO_2$  is adsorbing predominantly on the calcite as the results of the competitive adsorption of  $CO_2/H_2S$  mixture. All adsorption selectivity curves exhibit a downward trend when the system pressure is at a low level (around 7 MPa) and then stays at a relatively stable level as pressure increases, showing a better adsorption capacity of  $CO_2$  in calcite nanopores compared to  $H_2S$ .

The impact of CO<sub>2</sub> concentration on adsorption preference at 323.15 K is shown in Fig. 13(a). As the mole fraction of carbon dioxide increases, the adsorption selectivity becomes lower, it indicates that the CO<sub>2</sub> adsorption on the contact of calcite is stronger with a low mole fraction. Fig. 13(b) illustrates the adsorption selectivity of CO2 over H2S in nanopores at four different temperatures. We observed that the adsorption selectivity improves as temperature increases, which indicates that the proportion of CO<sub>2</sub> molecules in the first adsorption layer consistently exceeds that of H<sub>2</sub>S molecules, and the disparity in the ratio of these two molecules within the first adsorption layer widens with rising temperature. As elevated temperatures result in a reduction in the adsorption performance of gas molecules, it is conjectured that the adsorption ability of carbon dioxide on calcite surface degrades more slowly compared to H2S. Generally, the mole fraction of CO2 and the pressure enhance the adsorption capacity of CO<sub>2</sub> in the CO<sub>2</sub>/H<sub>2</sub>S combination, while the high temperature is reversed. While the adsorption selectivity of CO<sub>2</sub> over H<sub>2</sub>S and adsorption isotherms of the mixtures demonstrate that CO<sub>2</sub> adsorption dominates when temperatures > 323.15 K and the pressure in the range of 0-7 MPa, suggesting that CO2 is more suitable for the sequestration in shallower formations.

# 3.4. Impact of water content

The adsorption performance of CO<sub>2</sub> and H<sub>2</sub>S are simulated in

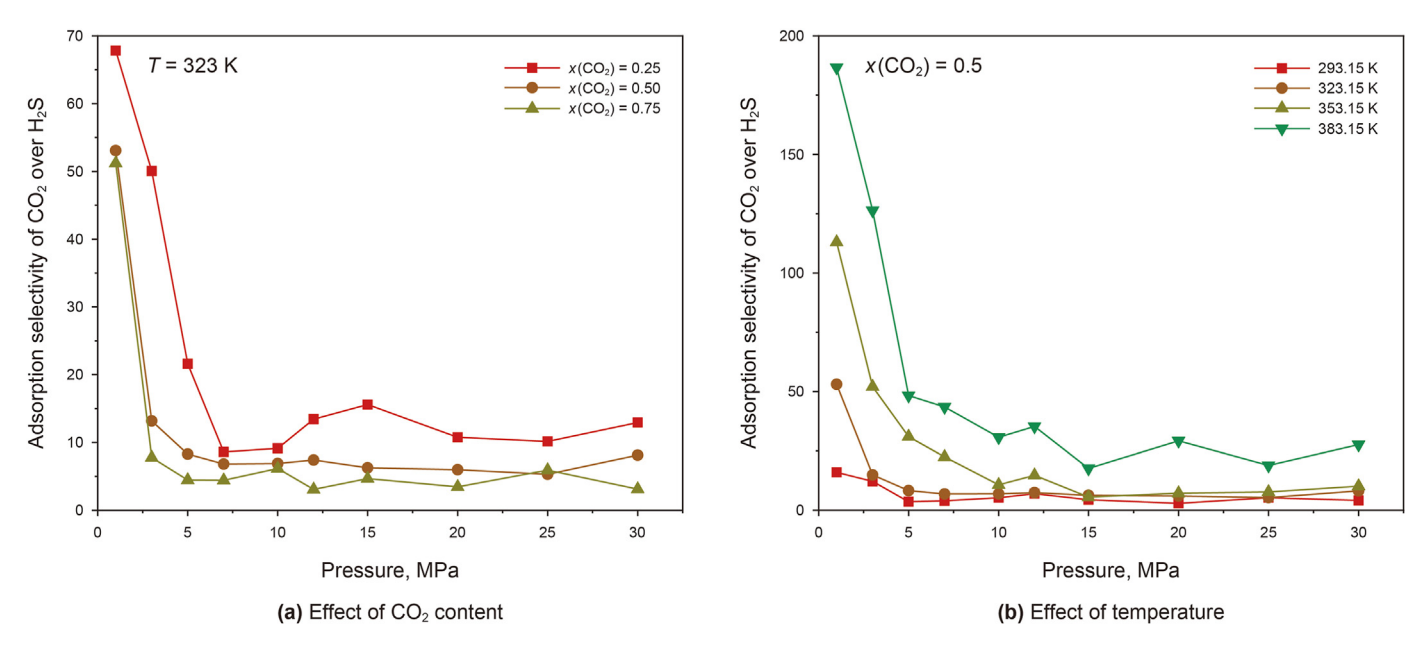


Fig. 13. Adsorption selectivity of CO<sub>2</sub> over H<sub>2</sub>S with the different mole fractions of CO<sub>2</sub> and temperatures.

calcite nanopores containing different water content. Noted that the mass fraction of water is calculated from the ratio of the  $H_2O$  mass to the total mass of calcite and water. The adsorption capacity of  $CO_2$  and  $H_2S$  with various water content at 323.15 K are plotted in Fig. 14. As the increase in water content in calcite nanopores, the  $CO_2$  and  $H_2S$  adsorption capability steadily declines. In more detail, the adsorption amount of  $CO_2$  and  $H_2S$  with water content of 2.61 wt% is reduced to 71.84% and 71.70%, respectively, compared to that in dry nanopores. According to Table 3, the influence of water content on the capacities of two gases for adsorption is generally coincident. Calcite nanopores were populated by clusters of water molecules and the  $H_2O$  molecule shows the highest priority in the adsorption performance in calcite nanopores than  $CO_2$  and  $H_2S$ . In other words, the  $H_2O$  molecules adsorbed in the calcite nanopores shield the two gas molecules.

**Table 3** The ratio of gas adsorption amount with water to that without water (323.15 K, 30 MPa).

Mass fraction of water, wt%	Ratio of gas adsorption amount, %		
	CO <sub>2</sub>	H <sub>2</sub> S	
0	100.00	100.00	
0.67	92.33	92.80	
1.32	85.13	85.99	
1.97	78.49	77.59	
2.61	71.84	71.70	

As shown in Fig. 15, in  $CO_2/H_2S$  mixture, the adsorption of  $CO_2$  in calcite nanopore without water content is slightly higher than that

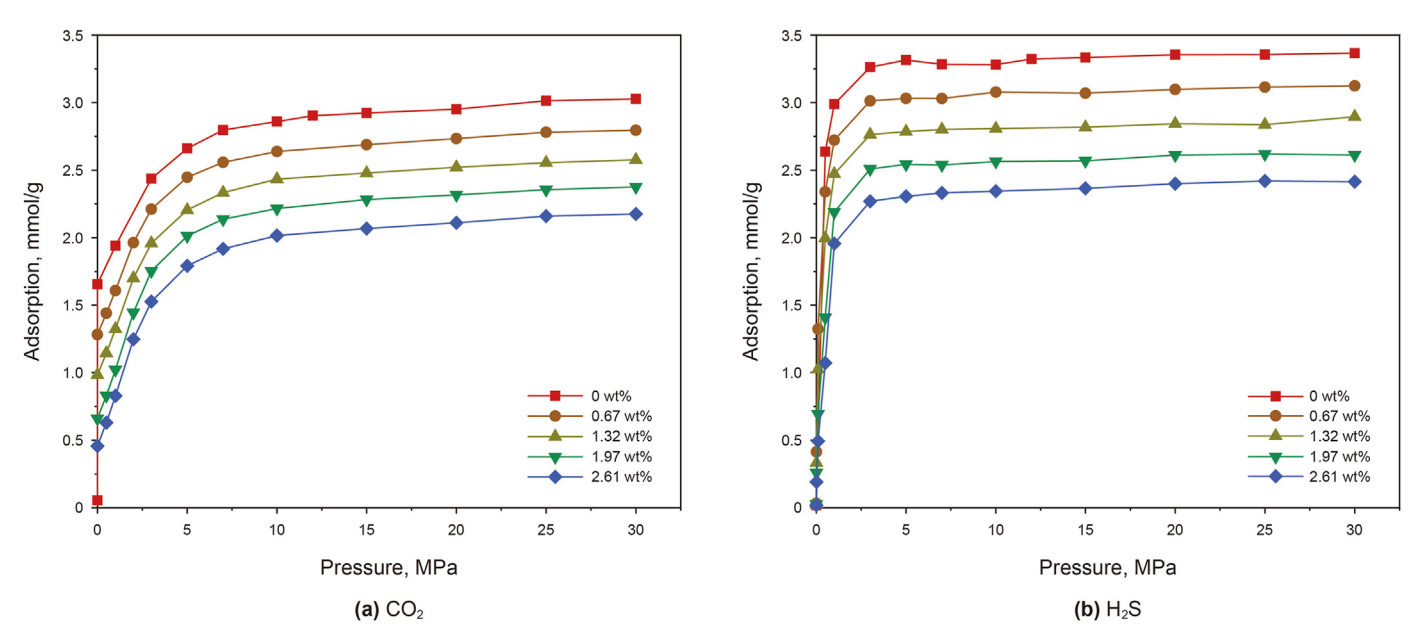


Fig. 14. Adsorption capacity of CO<sub>2</sub> and H<sub>2</sub>S with different water content (323.15 K).



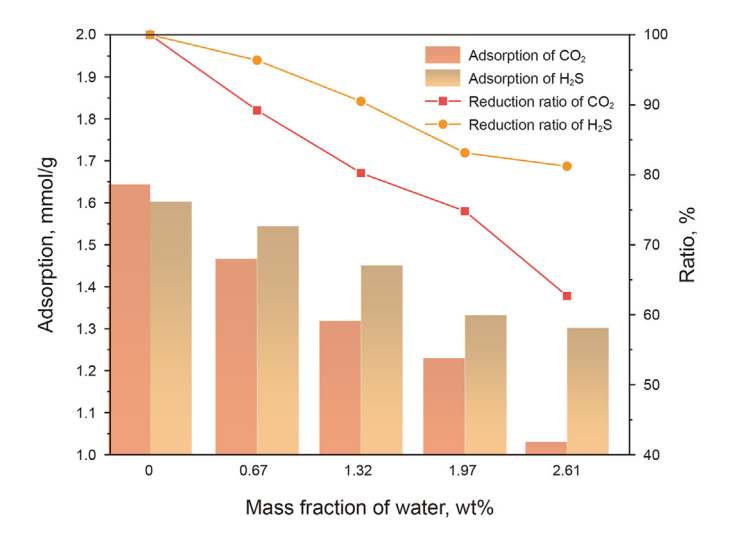


Fig. 15. The adsorption amount of  $CO_2$  and  $H_2S$  and the ratio of gas adsorption amount with different water content at  $x(CO_2) = 0.5$  (323.15 K, 30 MPa).

of  $H_2S$ . The adsorption of two gases declines as the  $H_2O$  content increases; the decline rate of  $CO_2$  adsorption is substantially greater than that of  $H_2S$ . When the water content is 2.61 wt%, the amount of  $CO_2$  and  $H_2S$  adsorbed drops to 62.70% and 81.22%, which illustrates that the adsorption performance of  $CO_2$  is more impacted by moisture in calcite nanopores compared with  $H_2S$ . It is mainly because both  $H_2O$  and  $CO_2$  tend to be adsorbed near the pore wall and  $CO_2$  originally adsorbed on the  $CaCO_3$  contact in the binary mixture is replaced by  $H_2O$ , which leads to a rapid decline in  $CO_2$  adsorption. Meanwhile, moisture has less impact on  $H_2S$  negatively located in the middle region of the nanopore. Hence, the existence of moisture limits  $CO_2$  absorption and sequestration in calcite-rich formations substantially.

#### 3.5. Implications for CO<sub>2</sub> sequestration

The co-injection of impurity gas will influence the total storage of CO2. Our study indicates that H2S can indeed reduce the adsorption of CO<sub>2</sub> in calcite pores, suggesting that H<sub>2</sub>S in injected CO<sub>2</sub> and native H<sub>2</sub>S in the formation will lessen the CO<sub>2</sub> storage in the calcite-rich formation. As has been mentioned, the increases in pressure and temperature have opposite effects on CO<sub>2</sub> adsorption. When CO<sub>2</sub> and impurity gas are stored in the reservoirs, pressure and temperature increase in tandem. Herein, we set up a series of depths with the pressure differences (1.0 MPa/100 m) and the geothermal differences (2.5 °C/100 m, the surface temperature is 20 °C) to optimize the depth for CO<sub>2</sub> sequestration. The adsorption ability of CO2 at various mole fractions and buried depths are shown in Fig. 16. As for pure CO<sub>2</sub>, its adsorption quantity quickly increases to its peak at roughly 2.90 mmol/g and then gradually declines as the depth of formation increases. It can be inferred that the intensifying effect of pressure dominates in shallower formations and then the weakening effect of temperature starts to take over the adsorption behavior when pure CO<sub>2</sub> dives into deeper formations. Hence, pure CO<sub>2</sub> is suggested to be sequestrated in the shallower formations, i.e. 500-1500 m.

Moisture has a detrimental effect on the ability of  $CO_2$  to be absorbed, reducing the adsorption amount by about 24%. Moisture significantly weakens  $CO_2$  adsorption and storage. As for  $CO_2/H_2S$  mixtures, the adsorption amount of  $CO_2$  increases as the buried depth increases, indicating that the pressure prevails over the competition with temperature. Meanwhile,  $CO_2$  adsorption amount

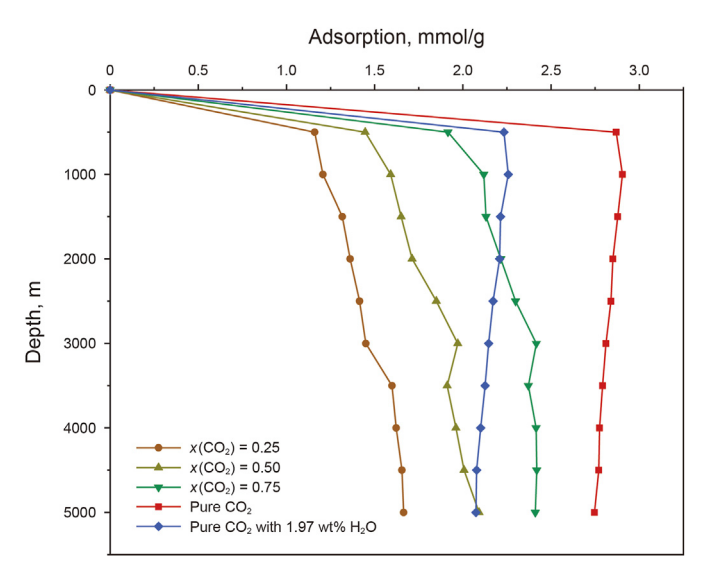


Fig. 16. Adsorption performance of  ${\rm CO_2}$  under different circumstances at various buried depths.

declines as the increase in  $H_2S$  mole fraction, indicating the detrimental effect of  $H_2S$  on  $CO_2$  storage capacity. Moreover, as the formation depth grows, the impact of  $H_2S$  lessens. It is suggested that  $CO_2$  containing  $H_2S$  should be stored in deeper formations.

#### 4. Conclusions

This work investigates the adsorption behavior of  $CO_2/H_2S$  mixture in calcite slit nanopores with GCMC simulations. The adsorption performance of  $CO_2$ ,  $H_2S$ , and their binary mixture in  $CaCO_3$  nanopores are simulated to estimate the impact of various factors. The following succinctly states the main conclusions.

- (1) In calcite nanopores, a rise in pressure enhances the adsorption ability of CO<sub>2</sub> and H<sub>2</sub>S, whereas the temperature is reversed. CO<sub>2</sub> shows stronger adsorption on the calcite surface and the two gases are both inclined to form double adsorption layers under higher adsorption amounts. Ca<sup>2+</sup> has a stronger interaction with CO<sub>2</sub> than H<sub>2</sub>S and the distance between CO<sub>2</sub> and Ca<sup>2+</sup> (2.26 Å) is less than that of H<sub>2</sub>S (3.62 Å). The interaction energy of calcite-CO<sub>2</sub> and calcite-H<sub>2</sub>S is -2072.14 kcal/mol and -1691.92 kcal/mol and electrostatic energy play a major role. The CO<sub>2</sub> adsorbed on the calcite surface shows an angle range of 15°-45° and the axis of H<sub>2</sub>S prefers to keep parallel or small angles with the calcite adsorption surface.
- (2) H<sub>2</sub>S reduces the adsorption amount of CO<sub>2</sub> in calcite nanopores due to the competitive adsorption of binary mixtures; a higher mole fraction of H<sub>2</sub>S causes less CO<sub>2</sub> adsorption. The adsorption amount of CO<sub>2</sub> and H<sub>2</sub>S in nanopores promotes as their mole fraction rises. CO<sub>2</sub> molecules preferentially occupy the position close to the nanopore wall and H<sub>2</sub>S molecules prefer to fill up the intermediate zone. The potential energy of CO<sub>2</sub> and H<sub>2</sub>S rises and falls with the promotion of gas mole proportion, which matches the trend of the average isosteric heat as the gas mole fraction increases.
- (3) The adsorption selectivity values of CO<sub>2</sub> over H<sub>2</sub>S exceeds 1, demonstrating the favorably adsorption of CO<sub>2</sub> in the competitive adsorption of the CO<sub>2</sub>/H<sub>2</sub>S mixture. The moisture in calcite nanopores can lessen the adsorption amount of CO<sub>2</sub> and H<sub>2</sub>S; the weakening effect gets stronger as the

water content increases. The weakening effect of water content on  $CO_2$  adsorption is significantly greater than that on  $H_2S$  adsorption in the binary mixture. Pure  $CO_2$  is suitable to be buried in the shallower formations i.e. 500-1500 m, whereas  $CO_2$  with  $H_2S$  should be settled in the reservoirs as deep as possible.

This work presents insights into the adsorption behavior of the  $CO_2/H_2S$  mixture and theoretical assistance for  $CO_2$  storage projects. In future research, a more in-depth investigation should also be performed on the diffusion, mass transfer behavior of  $CO_2$ , and its multi-component mixtures to support  $CO_2$  sequestration.

#### **CRediT authorship contribution statement**

**Cheng Qian:** Writing — original draft, Methodology, Investigation, Conceptualization. **Zhen-Hua Rui:** Supervision, Project administration. **Yue-Liang Liu:** Supervision, Data curation. **Kai Du:** Writing — review & editing, Data curation. **Chen Liu:** Visualization, Data curation. **Yang Zhao:** Writing — review & editing, Visualization, Investigation. **Xiao-Min Ma:** Software, Data curation.

# **Declaration of competing interest**

The authors declare that they have no known competing financial interests or personal relationships that could have appeared to influence the work reported in this paper.

#### Acknowledgments

We greatly acknowledge the financial support from the National Natural Science Foundation of China (Grant No. 52004320), the Science Foundation of China University of Petroleum, Beijing (No. 2462021QNXZ012, No. 2462022BJRC001, and No. 2462021YJRC012), and the funding from the State Key Laboratory of Petroleum Resources and Engineering (No. PRP/indep-1-2103).

# References

- Alpermann, T., Dietrich, M., Ostertag-Henning, C., 2016. Mineral trapping of a CO<sub>2</sub>/H<sub>2</sub>S mixture by hematite under initially dry hydrothermal conditions. Int. J. Greenh. Gas Control 51, 346–356. https://doi.org/10.1016/j.jiggc.2016.05.029.
- Bachu, S., Bennion, D.B., 2009. Chromatographic partitioning of impurities contained in a CO<sub>2</sub> stream injected into a deep saline aquifer: Part 1. Effects of gas composition and in situ conditions. Int. J. Greenh. Gas Control 3, 458–467. https://doi.org/10.1016/j.ijggc.2009.01.001.
- Bachu, S., Nordbotten, J.M., Celia, M.A., 2005. Evaluation of the spread of acid-gas plumes injected in deep saline aquifers in western Canada as an analogue for CO<sub>2</sub> injection into continental sedimentary basins. In: Rubin, E.S., Keith, D.W., Gilboy, C.F., Wilson, M., Morris, T., Gale, J., Thambimuthu, K. (Eds.), Greenhouse Gas Control Technologies 7. Elsevier Science Ltd, Oxford, pp. 479–487. https://doi.org/10.1016/B978-008044704-9/50049-5.
- Bolourinejad, P., Herber, R., 2014. Experimental and modeling study of salt precipitation during injection of CO<sub>2</sub> contaminated with H<sub>2</sub>S into depleted gas fields in the Northeast of The Netherlands. SPE J. 19, 1058—1068. https://doi.org/10.2118/164932-PA.
- Bui, M., Adjiman, C.S., Bardow, A., Anthony, E.J., Boston, A., Brown, S., Fennell, P.S., Fuss, S., Galindo, A., Hackett, L.A., 2018. Carbon capture and storage (CCS): the way forward. Energy Environ. Sci. 11, 1062–1176. https://doi.org/10.1039/ C7FE02342A.
- Chen, C., Chai, Z., Shen, W., Li, W., 2018. Effects of impurities on CO<sub>2</sub> sequestration in saline aquifers: perspective of interfacial tension and wettability. Ind. Eng. Chem. Res. 57, 371–379. https://doi.org/10.1021/acs.iecr.7b03873.
- Cholewinski, A., Dengis, J., Malkov, V., Leonenko, Y., 2016. Modeling of CO<sub>2</sub> injection into aquifers containing dissolved H<sub>2</sub>S. J. Nat. Gas Sci. Eng. 36, 1080–1086. https://doi.org/10.1016/j.jngse.2016.05.022.
- Clark, J.A., Santiso, E.E., 2018. Carbon sequestration through CO<sub>2</sub> foam-enhanced oil recovery: a green chemistry perspective. Engineering 4, 336–342. https://doi.org/10.1016/j.eng.2018.05.006.
- Cui, G., Wang, Y., Rui, Z., Chen, B., Ren, S., Zhang, L., 2018. Assessing the combined influence of fluid-rock interactions on reservoir properties and injectivity during CO<sub>2</sub> storage in saline aquifers. Energy 155, 281–296. https://doi.org/ 10.1016/j.energy.2018.05.024.

Cui, G., Pei, S., Rui, Z., Dou, B., Ning, F., Wang, J., 2021a. Whole process analysis of geothermal exploitation and power generation from a depleted hightemperature gas reservoir by recycling CO<sub>2</sub>. Energy 217, 119340. https:// doi.org/10.1016/j.energy.2020.119340.

- Cui, G., Yang, L., Fang, J., Qiu, Z., Wang, Y., Ren, S., 2021b. Geochemical reactions and their influence on petrophysical properties of ultra-low permeability oil reservoirs during water and CO<sub>2</sub> flooding. J. Petrol. Sci. Eng. 203, 108672. https:// doi.org/10.1016/j.petrol.2021.108672.
- Deng, X., Zhang, Q., Zhang, Z., Li, Q., Liu, X., 2022. Adsorption and diffusion behavior of CO<sub>2</sub>/H<sub>2</sub> mixture in calcite slit pores: a molecular simulation study. J. Mol. Liq. 346, 118306. https://doi.org/10.1016/j.molliq.2021.118306.
- Fazelabdolabadi, B., Alizadeh-Mojarad, A., 2016. On the adsorption and hydrodynamics behavior of H<sub>2</sub>S and CO<sub>2</sub> molecules in organic liquids inside nanoslit pores in vicinity of calcite {10 \(\tilde{1}\) 4} surface. J. Nat. Gas Sci. Eng. 28, 106—120. https://doi.org/10.1016/j.jngse.2015.11.023.
- Ghaderi, S.M., Keith, D.W., Lavoie, R., Leonenko, Y., 2011. Risk associated with H<sub>2</sub>S evolution in sour aquifers during CO<sub>2</sub> injection. Energy Proc. 4, 4117–4123. https://doi.org/10.1016/j.egypro.2011.02.355.
- Hu, W., Chen, C., Sun, J., Zhang, N., Zhao, J., Liu, Y., Ling, Z., Li, W., Liu, W., Song, Y., 2022. Three-body aggregation of guest molecules as a key step in methane hydrate nucleation and growth. Commun. Chem. 5, 33. https://doi.org/10.1038/s42004-022-00652-0
- Huang, X., Gu, L., Li, S., Du, Y., Liu, Y., 2022. Absolute adsorption of light hydrocarbons on organic-rich shale: an efficient determination method. Fuel 308, 121998. https://doi.org/10.1016/j.fuel.2021.121998.
- Hutcheon, I., 1999. Controls on the distribution of non-hydrocarbon gases in the Alberta Basin. Bull. Can. Petrol. Geol. 47, 573–593. https://doi.org/10.35767/ gscpgbull.47.4.573.
- Iglauer, S., 2017. CO<sub>2</sub>—water—rock wettability: variability, influencing factors, and implications for CO<sub>2</sub> geostorage. Accounts Chem. Res. 50, 1134—1142. https://doi.org/10.1021/acs.accounts.6b00602.
- International Energy Agenc, 2022. Global Energy Review: CO2 Emissions in 2021.
- Jayasekara, D.W., Ranjith, P.G., Wanniarachchi, W.A.M., Rathnaweera, T.D., 2020. Understanding the chemico-mineralogical changes of caprock sealing in deep saline CO<sub>2</sub> sequestration environments: a review study. J. Supercrit. Fluids 161, 104819. https://doi.org/10.1016/j.supflu.2020.104819.
- Ji, X., Zhu, C., 2013. Predicting possible effects of H<sub>2</sub>S impurity on CO<sub>2</sub> transportation and geological storage. Environ. Sci. Technol. 47, 55–62. https://doi.org/10.1021/es301292n
- Kamath, G., Potoff, J.J., 2006. Monte Carlo predictions for the phase behavior of H<sub>2</sub>S + *n*-alkane, H<sub>2</sub>S + CO<sub>2</sub>, CO<sub>2</sub> + CH<sub>4</sub> and H<sub>2</sub>S + CO<sub>2</sub> + CH<sub>4</sub> mixtures. Fluid Phase Equil. 246, 71–78. https://doi.org/10.1016/j.fluid.2006.05.011.
- Keith, D.W., Holmes, G., Angelo, D.S., Heidel, K., 2018. A process for capturing CO<sub>2</sub> from the atmosphere. Joule 2, 1573–1594. https://doi.org/10.1016/j.joule.2018.05.006.
- Kolle, J.M., Fayaz, M., Sayari, A., 2021. Understanding the effect of water on CO<sub>2</sub> adsorption. Chem. Rev. 121, 7280–7345. <a href="https://doi.org/10.1021/acs.chemrev.0c00762">https://doi.org/10.1021/acs.chemrev.0c00762</a>.
- Li, D., Jiang, X., 2020. Numerical investigation of convective mixing in impure CO<sub>2</sub> geological storage into deep saline aquifers. Int. J. Greenh. Gas Control 96, 103015. https://doi.org/10.1016/j.ijggc.2020.103015.
- Li, D., He, Y., Zhang, H., Xu, W., Jiang, X., 2017. A numerical study of the impurity effects on CO<sub>2</sub> geological storage in layered formation. Appl. Energy 199, 107–120. https://doi.org/10.1016/j.apenergy.2017.04.059.
- Li, D., Jiang, X., Zhong, Y., Liu, A., 2021a. Coupling effects of native H<sub>2</sub>S and different co-injected impurities on CO<sub>2</sub> sequestration in layered saline aquifers. J. Nat. Gas Sci. Eng. 88, 103846. https://doi.org/10.1016/j.jngse.2021.103846.
- Li, H., Yang, Z., Li, R., Zhou, T., Guo, H., Liu, X., Dai, Y., Hu, Z., Meng, H., 2021b. Mechanism of CO<sub>2</sub> enhanced oil recovery in shale reservoirs. Petrol. Sci. 18, 1788–1796. https://doi.org/10.1016/j.petsci.2021.09.040.
- Li, S., Liu, Y., Xue, L., Yang, L., Yuan, Z., 2022. A molecular insight into the effect of key ions on the detachment of crude oil from calcite surface: implication for low salinity water flooding in carbonate reservoirs. J. Petrol. Sci. Eng. 208, 109562. https://doi.org/10.1016/j.petrol.2021.109562.
- Liu, S., Ren, B., Li, H., Yang, Y., Wang, Z., Wang, B., Xu, J., Agarwal, R., 2022a. CO<sub>2</sub> storage with enhanced gas recovery (CSEGR): a review of experimental and numerical studies. Petrol. Sci. 19, 594–607. https://doi.org/10.1016/j.petsci.2021.12.009.
- Liu, Y., Hou, J., 2020. Selective adsorption of CO<sub>2</sub>/CH<sub>4</sub> mixture on clay-rich shale using molecular simulations. J. CO<sub>2</sub> Util. 39, 101143. https://doi.org/10.1016/ j.jcou.2020.02.013.
- Liu, Y., Rui, Z., 2022. A storage-driven CO<sub>2</sub> EOR for a net-zero emission target. Engineering 18, 79–87. https://doi.org/10.1016/j.eng.2022.02.010.
- Liu, Y., Li, H.A., Okuno, R., 2016. Measurements and modeling of interfacial tension for CO<sub>2</sub>/CH<sub>4</sub>/brine systems under reservoir conditions. Ind. Eng. Chem. Res. 55, 12358–12375. https://doi.org/10.1021/acs.iecr.6b02446.
- Liu, Y., Ma, X., Hou, J., 2019a. Comparing the effectiveness of SO<sub>2</sub> with CO<sub>2</sub> for replacing hydrocarbons from nanopores. Energy Fuels 33, 5200–5207. https:// doi.org/10.1021/acs.energyfuels.9b00995.
- Liu, Y., Ma, X., Li, H.A., Hou, J., 2019b. Competitive adsorption behavior of hydrocarbon(s)/CO<sub>2</sub> mixtures in a double-nanopore system using molecular simulations. Fuel 252, 612–621. https://doi.org/10.1016/j.fuel.2019.04.123.
- Liu, Y., Rui, Z., Yang, T., Dindoruk, B., 2022b. Using propanol as an additive to CO<sub>2</sub> for improving CO<sub>2</sub> utilization and storage in oil reservoirs. Appl. Energy 311, 118640. https://doi.org/10.1016/j.apenergy.2022.118640.

Lu, J., Mickler, P.J., Nicot, J.-P., Yang, C., Darvari, R., 2016. Geochemical impact of O<sub>2</sub> impurity in CO<sub>2</sub> stream on carbonate carbon-storage reservoirs. Int. J. Greenh. Gas Control 47, 159–175. https://doi.org/10.1016/j.ijggc.2016.01.039.

- Luo, L., Chu, L., Fwa, T.F., 2020. Molecular dynamics analysis of moisture effect on asphalt-aggregate adhesion considering anisotropic mineral surfaces. Appl. Surf. Sci. 527, 146830. https://doi.org/10.1016/j.apsusc.2020.146830.
- McQuaid, M.J., Sun, H., Rigby, D., 2004. Development and validation of COMPASS force field parameters for molecules with aliphatic azide chains. J. Comput. Chem. 25, 61–71. https://doi.org/10.1002/jcc.10316.
- Metz, B., Davidson, O., De Coninck, H.C., Loos, M., Meyer, L., 2005. IPCC Special Report on Carbon Dioxide Capture and Storage. Cambridge University Press, Cambridge.
- O'Neill, S., 2020. Global CO2 emissions level off in 2019, with a drop predicted in 2020. Engineering (Beijing, China) 6, 958. https://doi.org/10.1016/j.eng.2020.07.005.
- Shi, Y., Song, X., Shen, Z., Wang, G., Li, X., Zheng, R., Geng, L., Li, J., Zhang, S., 2018. Numerical investigation on heat extraction performance of a CO<sub>2</sub> enhanced geothermal system with multilateral wells. Energy 163, 38–51. https://doi.org/ 10.1016/j.energy.2018.08.060
- Sun, H., 1998. COMPASS: an ab initio force-field optimized for condensed-phase applications overview with details on alkane and benzene compounds. I. Phys. Chem. B 102, 7338–7364. https://doi.org/10.1021/jp980939v.
- Sun, H., Ren, P., Fried, J.R., 1998. The COMPASS force field: parameterization and validation for phosphazenes. Comput. Theor. Polym. Sci. 8, 229–246. https:// doi.org/10.1016/S1089-3156(98)00042-7.
- Sun, H., Jin, Z., Yang, C., Akkermans, R.L., Robertson, S.H., Spenley, N.A., Miller, S., Todd, S.M., 2016. Compass II: extended coverage for polymer and drug-like molecule databases. J. Mol. Model. 22, 1–10. https://doi.org/10.1007/s00894-016-2909-0
- Sun, J., Chen, Z., Wang, X., Zhang, Y., Qin, Y., Chen, C., Li, W., Zhou, W., 2023. Displacement characteristics of CO<sub>2</sub> to CH<sub>4</sub> in heterogeneous surface slit pores. Energy Fuels 37, 2926–2944. https://doi.org/10.1021/acs.energyfuels.2c03610.
- Sun, W., Wang, H., 2020. Moisture effect on nanostructure and adhesion energy of asphalt on aggregate surface: a molecular dynamics study. Appl. Surf. Sci. 510, 145435. https://doi.org/10.1016/j.apsusc.2020.145435.
- Talman, S., 2015. Subsurface geochemical fate and effects of impurities contained in a CO<sub>2</sub> stream injected into a deep saline aquifer: what is known. Int. J. Greenh.

- Gas Control 40, 267-291. https://doi.org/10.1016/j.ijggc.2015.04.019.
- Tyne, R.L., Barry, P.H., Lawson, M., Byrne, D.J., Warr, O., Xie, H., Hillegonds, D.J., Formolo, M., Summers, Z.M., Skinner, B., 2021. Rapid microbial methanogenesis during CO<sub>2</sub> storage in hydrocarbon reservoirs. Nature 600, 670–674. https://www.nature.com/articles/s41586-021-04153-3.
- Vilarrasa, V., Carrera, J., 2015. Geologic carbon storage is unlikely to trigger large earthquakes and reactivate faults through which CO<sub>2</sub> could leak. Proc. Natl. Acad. Sci. USA 112, 5938–5943. https://doi.org/10.1073/pnas.1413284112.
- Wang, J., Wang, Z., Ryan, D., Lan, C., 2015. A study of the effect of impurities on CO<sub>2</sub> storage capacity in geological formations. Int. J. Greenh. Gas Control 42, 132–137. https://doi.org/10.1016/j.jiggc.2015.08.002.
- Wang, T., Tian, S., Li, G., Sheng, M., 2018. Selective adsorption of supercritical carbon dioxide and methane binary mixture in shale kerogen nanopores. J. Nat. Gas Sci. Eng. 50, 181–188. https://doi.org/10.1016/j.jngse.2017.12.002.
- Wang, T., Tian, S., Liu, Q., Li, G., Sheng, M., Ren, W., Zhang, P., 2021. Pore structure characterization and its effect on methane adsorption in shale kerogen. Petrol. Sci. 18, 565–578. https://doi.org/10.1007/s12182-020-00528-9.
- Wang, Z., Wang, J., Lan, C., He, I., Ko, V., Ryan, D., Wigston, A., 2016. A study on the impact of SO<sub>2</sub> on CO<sub>2</sub> injectivity for CO<sub>2</sub> storage in a Canadian saline aquifer. Appl. Energy 184, 329–336. https://doi.org/10.1016/j.apenergy.2016.09.067.
- Wei, N., Li, X., Wang, Y., Zhu, Q., Liu, S., Liu, N., Su, X., 2015. Geochemical impact of aquifer storage for impure CO<sub>2</sub> containing O<sub>2</sub> and N<sub>2</sub>: tongliao field experiment. Appl. Energy 145, 198–210. https://doi.org/10.1016/j.apenergy.2015.01.017.
- Yu, Y., Yang, G., Cheng, F., Yang, S., 2021. Effects of impurities N<sub>2</sub> and O<sub>2</sub> on CO<sub>2</sub> storage efficiency and costs in deep saline aquifers. J. Hydrol. 597, 126187. https://doi.org/10.1016/j.jhydrol.2021.126187.
- Zhang, M., Zhan, S., Jin, Z., 2020. Recovery mechanisms of hydrocarbon mixtures in organic and inorganic nanopores during pressure drawdown and CO<sub>2</sub> injection from molecular perspectives. Chem. Eng. J. 382, 122808. https://doi.org/10.1016/ i.cei.2019.122808.
- Zhang, W., Xu, T., Li, Y., 2011. Modeling of fate and transport of coinjection of H<sub>2</sub>S with CO<sub>2</sub> in deep saline formations. J. Geophys. Res. Solid Earth 116. https://doi.org/10.1029/2010/B007652.
- Zhang, Z., Zhang, G., Mo, C., 2021. Study on the microscopic adsorption of sulfur molecules onto {10 ī 4} calcite surface. Colloids Surf. A Physicochem. Eng. Asp. 630, 127630. https://doi.org/10.1016/j.colsurfa.2021.127630.